Variable Eddington Factor Method for S_N Equations with Discontinuous Galerkin Spatial Discretization and a Mixed Finite-Element Balance Equation

Samuel S. Olivier, Jim E. Morel

Department of Nuclear Engineering
Texas A&M University
College Station, TX 77843

Abstract

We present the Variable Eddington Factor (VEF) method, a nonlinear Discrete Ordinates Source Iteration scheme that relaxes the consistency requirement of the transport and acceleration steps' spatial discretization. The method was applied to the 1-D, one-group neutron transport equation with Lumped Linear Discontinuous Galerkin (LLDG) transport and the constant-linear Mixed Finite-Element Method (MFEM) drift-diffusion acceleration. Methods for increased consistency between the transport and acceleration steps are also presented. The VEF method exhibited second-order convergence as expected from the orders of accuracy of LLDG and MFEM in isolation, accelerated source iterations as well as consistently differenced S_2SA, and preserved the thick diffusion limit. In addition, the difference between the transport and acceleration steps' solution was shown to converge as the mesh was refined.

Keywords
Variable Eddington Factor, Source Iteration Acceleration, Lumped Linear Discontinuous Galerkin, Mixed Finite Element Method

Running Head
Variable Eddington Factor Method

Corresponding Author
Samuel S. Olivier, email: *smsolivier@gmail.com*.

1 Introduction

The Variable Eddington Factor (VEF) method, also known as Quasi-Diffusion (QD), was one of the first nonlinear methods for accelerating source iterations in S_N calculations [1]. It is comparable in effectiveness to both linear and nonlinear forms of Diffusion Synthetic Acceleration (DSA), but it offers much more flexibility than DSA. Stability can only be guaranteed with DSA if the diffusion equation is differenced in a manner consistent with that of the S_N equations [2]. Modern S_N codes often use advanced discretization schemes such as Discontinuous Galerkin (DG) since classic discretization schemes such as step and diamond are not suitable for radiative transfer calculations in the High Energy Density Laboratory Physics (HEDLP) regime or coupled electron-photon calculations. Diffusion discretizations consistent with DG S_N discretizations cannot actually be expressed in diffusion form, but rather must be expressed in first-order or P_1 form, and are much more difficult to solve than standard diffusion discretizations [3]. Considerable effort has gone into the development of "partially consistent" diffusion discretizations that yield a stable DSA algorithm with some degree of degraded effectiveness, but such discretizations are also generally difficult to develop [4, 5, 6].

A great advantage of the VEF method is that the drift-diffusion equation that accelerates the S_N source iterations can be discretized in any valid manner without concern for consistency with the S_N discretization. When the VEF drift-diffusion equation is discretized in a way that is "non-consistent," the S_N and VEF drift-diffusion solutions for the scalar flux do not necessarily become identical when the iterative process converges. However, they do become identical in the limit as the spatial mesh is refined, and the difference between the two solutions is proportional to the spatial truncation errors associated with the S_N and drift-diffusion discretizations. In general, the order accuracy of the S_N and VEF drift-diffusion solutions will be the lowest order accuracy of their respective independent discretizations. Although the S_N solution obtained with such a "non-consistent" VEF method is not conservative, the VEF drift-diffusion solution is in fact conservative. This is particularly useful in multiphysics calculations where the low-order VEF equation can be coupled to the other physics components rather than the high-order S_N equations. Another advantage of the non-consistent approach is that even if the S_N spatial discretization scheme does not preserve the thick diffusion limit [7], that limit will generally be preserved using the VEF method.

The purpose of this paper is to investigate the application of the VEF method to the 1-D S_N equations discretized with the Lumped Linear Discontinuous Galerkin (LLDG) method and the drift-diffusion equation discretized using the constant-linear Mixed Finite-Element Method (MFEM). To our knowledge, this combination has not been previously investigated. Our motivation for this investigation is that MFEM methods are now being used for high-order hydrodynamics calculations [8]. A radiation transport method compatible with MFEM methods is clearly desirable for developing a MFEM radiation-hydrodynamics code. Such a code would combine thermal radiation transport with hydrodynamics. However, MFEM methods are inappropriate for the standard first-order form of the transport equation. Thus, the use of the VEF method with a DG S_N discretization and a MFEM drift-diffusion discretization suggests itself.

Here we define a VEF method that should exhibit second-order accuracy since both the transport and drift-diffusion discretizations are second-order accurate in isolation. In addition, our VEF method should preserve the thick diffusion limit, which is essential for radiative transfer calculations in the HEDLP regime. We use the lumped rather than the standard Linear Discontinuous Galerkin discretization because lumping yields a much more robust scheme, and robustness is essential for radiative transfer calculations in the HEDLP regime. Because this is an initial study, we simplify the investigation by considering only the one-group neutron transport equation rather than the full radiative transfer equations, which include a material temperature equation as well as the radiation transport equation. The vast majority of relevant properties of a VEF method for radiative transfer can be tested with an analogous method for one-group neutron transport. Furthermore, a high order DG-MFEM VEF method could be of interest for neutronics in addition to radiative transfer calculations. A full investigation for radiative transfer calculations will be carried out in a future study.

The remainder of this paper is organized as follows. First, we describe the VEF method analytically. Then, we describe our discretized S_N equations, followed by a description of the discretized VEF drift-diffusion equation. Methods for increased consistency between LLDG and MFEM are also presented. We next give computational results. We show the acceleration properties of the VEF method, compare the convergence rates of unaccelerated Source Iteration, the VEF method, and consistently differenced S_2SA, present the VEF methods' experimentally-determined order of accuracy, compare the S_N and drift-diffusion solutions as the mesh is refined, and show that this method preserves the thick diffusion limit. Finally, we give conclusions and recommendations for future work.

2 The VEF Method

2.1 The Algorithm

Here, we describe the VEF method for a planar geometry, fixed-source problem:

$$\mu \frac{\partial \psi}{\partial x}(x, \mu) + \sigma_t(x)\psi(x, \mu) = \frac{\sigma_s(x)}{2} \int_{-1}^{1} \psi(x, \mu') \, \mathrm{d}\mu' + \frac{Q(x)}{2} \, , \tag{1}$$

where $\mu = \cos\theta$ is the cosine of the angle of flight, θ, relative to the x–axis, $\sigma_t(x)$ and $\sigma_s(x)$ the total and scattering macroscopic cross sections, $Q(x)$ the isotropic fixed-source and $\psi(x,\mu)$ the angular flux. Applying the Discrete Ordinates (S_N) angular discretization yields the following set of N coupled, ordinary differential equations:

$$\mu_n \frac{\mathrm{d}\psi_n}{\mathrm{d}x}(x) + \sigma_t(x)\psi_n(x) = \frac{\sigma_s(x)}{2}\phi(x) + \frac{Q(x)}{2}\,, \quad 1 \le n \le N\,, \tag{2}$$

where $\psi_n(x) = \psi(x,\mu_n)$ is the angular flux in direction μ_n. The μ_n are stipulated by an N-point Gauss quadrature rule such that the scalar flux, $\phi(x)$, is numerically integrated as follows:

$$\phi(x) = \sum_{n=1}^{N} w_n \psi_n(x)\,, \tag{3}$$

where w_n is the quadrature weight corresponding to μ_n.

The VEF method begins by solving Eq. 2 while lagging the scattering term. This is called a Source Iteration (SI), and is represented as follows:

$$\mu_n \frac{\mathrm{d}}{\mathrm{d}x}\psi_n^{\ell+1/2}(x) + \sigma_t(x)\psi_n^{\ell+1/2}(x) = \frac{\sigma_s(x)}{2}\phi^{\ell}(x) + \frac{Q(x)}{2}\,, \quad 1 \le n \le N\,, \tag{4}$$

where ℓ is the iteration index. The scalar flux used in the scattering term, ϕ^ℓ, is assumed to be known either from the previous iteration or from the initial guess if $\ell = 0$. The use of a half-integral index indicates that SI is the first of a two-step iteration scheme. If one is only doing SI without acceleration, the second step would simply be to set the final scalar flux iterate to the iterate after the source iteration:

$$\phi(x)^{\ell+1} = \phi(x)^{\ell+1/2}\,. \tag{5}$$

However, SI is slow to converge in optically thick and highly scattering systems. This is the motivation for accelerating SI using the VEF method.

The second iterative step of the VEF method is to obtain a final "accelerated" iterate for the scalar flux by solving the VEF drift-diffusion equation using angular flux shape information from the source iteration step:

$$-\frac{\mathrm{d}}{\mathrm{d}x}\frac{1}{\sigma_t(x)}\frac{\mathrm{d}}{\mathrm{d}x}\left[\langle\mu^2\rangle^{\ell+1/2}(x)\phi^{\ell+1}(x)\right] + \sigma_a(x)\phi^{\ell+1}(x) = Q(x)\,, \tag{6}$$

where the Eddington factor is given by

$$\langle\mu^2\rangle^{\ell+1/2}(x) = \frac{\int_{-1}^{1}\mu^2\psi^{\ell+1/2}(x,\mu)\,\mathrm{d}\mu}{\int_{-1}^{1}\psi^{\ell+1/2}(x,\mu)\,\mathrm{d}\mu}\,. \tag{7}$$

Note that the Eddington factor depends only upon the angular shape of the angular flux, and not its magnitude. This drift-diffusion equation is derived by first taking the first two angular moments of Eq. 2:

$$\frac{\mathrm{d}}{\mathrm{d}x}J(x) + \sigma_a(x)\phi(x) = Q(x)\,, \tag{8a}$$

$$\frac{\mathrm{d}}{\mathrm{d}x}\left[\langle\mu^2\rangle(x)\phi(x)\right] + \sigma_t(x)J(x) = 0\,, \tag{8b}$$

where $J(x)$ is the current. Then Eq. 8b is solved for $J(x)$, and this expression is then substituted into Eq. 8a. Performing a SI, computing the Eddington factor from the SI angular flux iterate, and then solving the drift-diffusion equation to obtain a new scalar flux iterate completes one accelerated iteration. These iterations are repeated until convergence of the scalar flux is achieved.

Acceleration occurs because the angular shape of the angular flux, and thus the Eddington factor, converges much faster than the scalar flux. In addition, the solution of the drift-

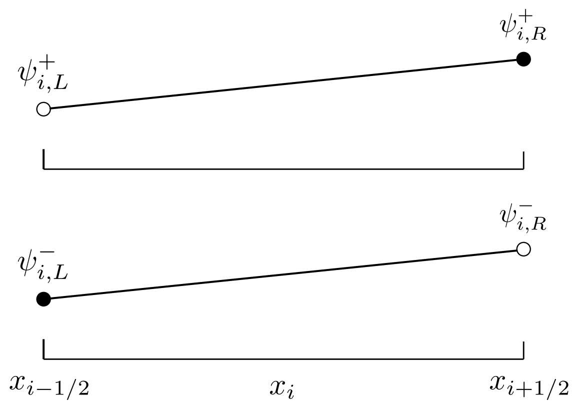

Figure 1: The distribution of unknowns in an LLDG cell. The superscript + and − indicate the angular fluxes for $\mu_n > 0$ and $\mu_n < 0$, respectively.

diffusion equation includes scattering. This inclusion compensates lagging the scattering term in the SI step.

The VEF method allows the S_N equations and drift-diffusion equations to be solved with arbitrarily different spatial discretization methods. The following sections present the application of the Lumped Linear Discontinuous Galerkin (LLDG) spatial discretization to the S_N equations and the constant-linear Mixed Finite-Element Method (MFEM) to the VEF drift-diffusion equation.

2.2 Lumped Linear Discontinuous Galerkin S_N

The spatial grid and distribution of unknowns for an LLDG cell are shown in Fig. 1. We assume a computational domain of length x_b discretized into I cells. The cell centers are integral and the cell edges are half integral. The two unknowns in each cell for each discrete angle are the left and right edge discontinuous angular fluxes, $\psi^{\ell+1/2}_{n,i,L}$ and $\psi^{\ell+1/2}_{n,i,R}$. These values are uniquely defined by upwinding:

$$\psi_{n,i-1/2}^{\ell+1/2} = \begin{cases} \psi_{n,i-1,R}^{\ell+1/2}\,, & \mu_n > 0 \\ \psi_{n,i,L}^{\ell+1/2}\,, & \mu_n < 0 \end{cases}\,, \tag{9a}$$

$$\psi_{n,i+1/2}^{\ell+1/2} = \begin{cases} \psi_{n,i,R}^{\ell+1/2}\,, & \mu_n > 0 \\ \psi_{n,i+1,L}^{\ell+1/2}\,, & \mu_n < 0 \end{cases}\,. \tag{9b}$$

The angular flux dependence within cells is linear and given in cell i by

$$\psi_{n,i}^{\ell+1/2}(x) = \psi_{n,i,L}^{\ell+1/2} B_{i,L}(x) + \psi_{n,i,R}^{\ell+1/2} B_{i,R}(x)\,, \quad x \in (x_{i-1/2}, x_{i+1/2}), \tag{10}$$

where

$$B_{i,L}(x) = \begin{cases} \frac{x_{i+1/2}-x}{x_{i+1/2}-x_{i-1/2}}\,, & x \in [x_{i-1/2}, x_{i+1/2}] \\ 0\,, & \text{otherwise} \end{cases}\,, \tag{11a}$$

$$B_{i,R}(x) = \begin{cases} \frac{x-x_{i-1/2}}{x_{i+1/2}-x_{i-1/2}}\,, & x \in [x_{i-1/2}, x_{i+1/2}] \\ 0\,, & \text{otherwise} \end{cases}\,, \tag{11b}$$

are the LLDG basis functions. The cell centered angular flux is the average of the left and right discontinuous edge fluxes:

$$\psi_{n,i}^{\ell+1/2} = \frac{1}{2}\left(\psi_{n,i,L}^{\ell+1/2} + \psi_{n,i,R}^{\ell+1/2}\right)\,. \tag{12}$$

The unlumped Linear Discontinuous Galerkin discretization for Eq. 4 is obtained by substituting $\psi_{n,i}^{\ell+1/2}(x)$ from Eq. 10 into Eq. 4, sequentially multiplying the resultant equation by each basis function, and integrating over each cell with integration by parts of the spatial derivative term. The lumped discretization equations are obtained simply by performing all volumetric integrals (after formal integration by parts of the spatial derivative term) using trapezoidal-rule quadrature. The LLDG discretization of Eq. 4 is given by:

$$\mu_n \left(\psi_{n,i}^{\ell+1/2} - \psi_{n,i-1/2}^{\ell+1/2}\right) + \frac{\sigma_{t,i}h_i}{2}\psi_{n,i,L}^{\ell+1/2} = \frac{\sigma_{s,i}h_i}{4}\phi_{i,L}^{\ell} + \frac{h_i}{4}Q_{i,L}\,, \tag{13a}$$

$$\mu_n \left(\psi_{n,i+1/2}^{\ell+1/2} - \psi_{n,i}^{\ell+1/2}\right) + \frac{\sigma_{t,i}h_i}{2}\psi_{n,i,R}^{\ell+1/2} = \frac{\sigma_{s,i}h_i}{4}\phi_{i,R}^{\ell} + \frac{h_i}{4}Q_{i,R}\,, \tag{13b}$$

where h_i, $\sigma_{t,i}$, $\sigma_{s,i}$, and $Q_{i,L/R}$ are the cell width, total cross section, scattering cross section and discontinuous fixed source in cell i. The discontinuous scalar fluxes, $\phi_{i,L/R}^{\ell}$, are assumed to be known from the drift-diffusion step of the previous iteration or the initial guess when $\ell = 0$. Equations 9a, 9b, 12, 13a, and 13b can be combined and rewritten as follows

$$\begin{bmatrix} \mu_n + \sigma_{t,i}h_i & \mu_n \\ -\mu_n & \sigma_{t,i} + \mu_n \end{bmatrix} \begin{bmatrix} \psi_{n,i,L}^{\ell+1/2} \\ \psi_{n,i,R}^{\ell+1/2} \end{bmatrix} = \begin{bmatrix} \frac{\sigma_{s,i}h_i}{2}\phi_{i,L}^{\ell} + \frac{h_i}{2}Q_{i,L} + 2\mu_n\psi_{n,i-1,R}^{\ell+1/2} \\ \frac{\sigma_{s,i}h_i}{2}\phi_{i,R}^{\ell} + \frac{h_i}{2}Q_{i,R} \end{bmatrix}, \tag{14}$$

for sweeping from left to right ($\mu_n > 0$) and

$$\begin{bmatrix} -\mu_n + \sigma_{t,i}h_i & \mu_n \\ -\mu_n & -\mu_n + \sigma_{t,i}h_i \end{bmatrix} \begin{bmatrix} \psi_{n,i,L}^{\ell+1/2} \\ \psi_{n,i,R}^{\ell+1/2} \end{bmatrix} = \begin{bmatrix} \frac{\sigma_{s,i}h_i}{2}\phi_{i,L}^{\ell} + \frac{h_i}{2}Q_{i,L} \\ \frac{\sigma_{s,i}h_i}{2}\phi_{i,R}^{\ell} + \frac{h_i}{2}Q_{i,R} - 2\mu_n\psi_{n,i+1,L}^{\ell+1/2} \end{bmatrix}, \tag{15}$$

for sweeping from right to left ($\mu_n < 0$), respectively. The right hand sides of Eqs. 14 and 15 are known as the scalar flux from the previous iteration, the fixed source, and the angular flux entering from the downwind cell are all known. By supplying the flux entering the left side of the first cell, the solution for $\mu_n > 0$ can be propagated from left to right by solving

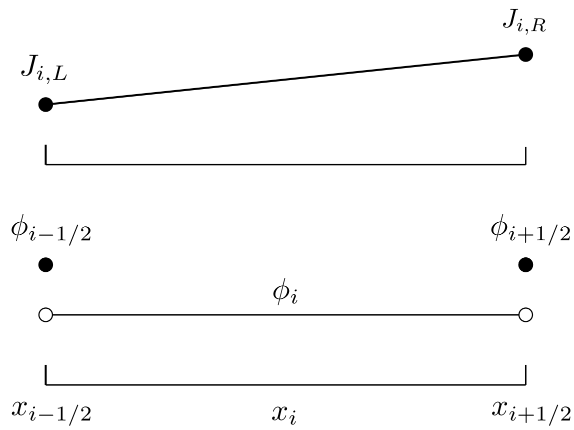

Figure 2: The distribution of unknowns in cell i for MFEM.

Eq. 14. Similarly, supplying the incident flux on the right boundary allows the solution for $\mu_n < 0$ to be propagated from right to left with Eq. 15. The Variable Eddington Factors needed in the drift-diffusion acceleration step are computed at the cell edges as follows:

$$\langle \mu^2 \rangle_{i\pm 1/2}^{\ell+1/2} = \frac{\sum_{n=1}^{N} \mu_n^2 \psi_{n,i\pm 1/2}^{\ell+1/2} w_n}{\sum_{n=1}^{N} \psi_{n,i\pm 1/2}^{\ell+1/2} w_n}\,, \tag{16}$$

where the $\psi_{n,i\pm 1/2}^{\ell+1/2}$ are defined by Eqs. 9a and 9b. The Eddington factors are computed within cell i as follows:

$$\langle \mu^2 \rangle^{\ell+1/2}(x) = \frac{\sum_{n=1}^{N} \mu_n^2 \psi_n^{\ell+1/2}(x) w_n}{\sum_{n=1}^{N} \psi_n^{\ell+1/2}(x) w_n}\,, \quad x \in (x_{i-1/2}, x_{i+1/2}), \tag{17}$$

where $\psi_n^{\ell+1/2}(x)$ is defined by Eq. 10.

2.3 Mixed Finite-Element Method for VEF Equation

We apply the MFEM method to Eqs. 8a and 8b and then eliminate the currents to obtain a discretization for Eq. 6. In this method, the grid is identical to that used in the LLDG S_N

discretization. The unknowns in an MFEM cell are depicted in Fig. 2. In MFEM, separate basis functions are used for the scalar flux and current. The scalar flux is constant within the cell with discontinuous jumps at the cell edges and the current is a linear function defined by:

$$J_i(x) = J_{i,L} B_{i,L}(x) + J_{i,R} B_{R,i}(x) \,, \tag{18}$$

where $J_{i,L/R}$ are the currents at the left and right edges of the cell, and the basis functions are identical to those defined by Eqs. 11a and 11b for the LLDG S_N discretization. The constant-linear MFEM yields second order accuracy for both the scalar flux and the current.

The MFEM representation yields five unknowns per cell: $\phi_{i-1/2}$, ϕ_i, $\phi_{i+1/2}$, $J_{i,L}$, and $J_{i,R}$. However, each edge flux on the mesh interior is shared by two cells, so with I cells there are I cell-center scalar fluxes, $2I$ currents, and $2I-1$ interior-mesh cell-edge scalar fluxes, and 2 boundary cell-edge scalar fluxes. An equation for ϕ_i is found by integrating Eq. 8a over cell i:

$$J_{i,R} - J_{i,L} + \sigma_{a,i} h_i \phi_i = Q_i h_i \,, \tag{19}$$

where $\sigma_{a,i}$ and Q_i are the absorption cross section and source in cell i. Equations for $J_{i,L/R}$ are found by multiplying Eq. 8b by $B_{i,L/R}$ and integrating over cell i:

$$-\langle \mu^2 \rangle_{i-1/2} \phi_{i-1/2} + \langle \mu^2 \rangle_i \phi_i + \sigma_{t,i} h_i \left(\frac{1}{3} J_{i,L} + \frac{1}{6} J_{i,R} \right) = 0 \,, \tag{20a}$$

$$\langle \mu^2 \rangle_{i+1/2} \phi_{i+1/2} - \langle \mu^2 \rangle_i \phi_i + \sigma_{t,i} h_i \left(\frac{1}{6} J_{i,L} + \frac{1}{3} J_{i,R} \right) = 0 \,, \tag{20b}$$

where the fixed source has been assumed to be isotropic. All Eddington factors are computed using the angular fluxes from the LLDG S_N step. Note that $\langle \mu^2 \rangle_{i\pm 1/2}$ denotes cell edge Eddington factors, while $\langle \mu^2 \rangle_i$ denotes an average over cell i of the Eddington factors. The edge Eddington factors are defined by Eq. 16, while the Eddington factors within each cell are defined by Eq. 17. We stress that evaluating Eq. 17 at $x_{i\pm1/2}$ does not yield $\langle\mu^2\rangle_{i\pm1/2}$ because of the upwinding used to define the cell edge angular fluxes. The spatial dependence of the Eddington factors within each cell takes the form of a rational polynomial prompting the use of numerical quadrature to compute the average. Two point Gauss quadrature was used:

$$\langle\mu^2\rangle_i = \frac{1}{2}\left[\langle\mu^2\rangle(x^G_{i,L}) + \langle\mu^2\rangle(x^G_{i,R})\right] \tag{21}$$

where

$$x^G_{i,L/R} = \frac{x_{i+1/2} + x_{i-1/2}}{2} \mp \frac{h_i}{2\sqrt{3}}\,. \tag{22}$$

Eliminating $J_{i,R}$ from Eq. 20a and $J_{i,L}$ from Eq. 20b yields:

$$J_{i,L} = \frac{-2}{\sigma_{t,i}h_i}\left\{2\left[\langle\mu^2\rangle_i\phi_i - \langle\mu^2\rangle_{i-1/2}\phi_{i-1/2}\right] - \left[\langle\mu^2\rangle_{i+1/2}\phi_{i+1/2} - \langle\mu^2\rangle_i\phi_i\right]\right\}, \tag{23a}$$

$$J_{i,R} = \frac{-2}{\sigma_{t,i}h_i}\left\{2\left[\langle\mu^2\rangle_{i+1/2}\phi_{i+1/2} - \langle\mu^2\rangle_i\phi_i\right] - \left[\langle\mu^2\rangle_i\phi_i - \langle\mu^2\rangle_{i-1/2}\phi_{i-1/2}\right]\right\}. \tag{23b}$$

An equation for $\phi_{i+1/2}$ on the mesh interior is found by enforcing continuity of current at the cell edges:

$$J_{i,R} = J_{i+1,L}\,. \tag{24}$$

Using the definitions of $J_{i,L}$ and $J_{i,R}$ from Eqs. 23a and 23b in the balance equation (Eq. 19) and continuity equation (Eq. 24) yields equations for all cell-center fluxes and interior-mesh cell-edge fluxes. The resulting balance and continuity equations are:

$$-\frac{6}{\sigma_{t,i}h_i}\langle\mu^2\rangle_{i-1/2}\phi_{i-1/2} + \left(\frac{12}{\sigma_{t,i}h_i}\langle\mu^2\rangle_i + \sigma_{a,i}h_i\right)\phi_i - \frac{6}{\sigma_{t,i}h_i}\langle\mu^2\rangle_{i+1/2}\phi_{i+1/2} = Q_i h_i\,, \tag{25a}$$

$$
\begin{aligned}
-\frac{2}{\sigma_{t,i}h_i}\langle\mu^2\rangle_{i-1/2}\phi_{i-1/2} + \frac{6}{\sigma_{t,i}h_i}\langle\mu^2\rangle_i\phi_i - 4\left(\frac{1}{\sigma_{t,i}h_i} + \frac{1}{\sigma_{t,i+1}h_{i+1}}\right)\langle\mu^2\rangle_{i+1/2}\phi_{i+1/2} \\
+ \frac{6}{\sigma_{t,i+1}h_{i+1}}\langle\mu^2\rangle_{i+1}\phi_{i+1} - \frac{2}{\sigma_{t,i+1}h_{i+1}}\langle\mu^2\rangle_{i+3/2}\phi_{i+3/2} = 0\,. \quad (25b)
\end{aligned}
$$

The equations for the outer boundary fluxes, $\phi_{1/2}$ and $\phi_{I+1/2}$, involve boundary conditions together with continuity conditions. For instance, the equation for $\phi_{1/2}$ is

$$
J_{1,L} = J_{1/2}\,, \tag{26}
$$

where $J_{1,L}$ is defined in Eq. 23a, and $J_{1/2}$ is the left boundary current defined by a boundary condition. For a reflective condition,

$$
J_{1/2} = 0\,. \tag{27}
$$

For a source condition,

$$
J_{1/2} = 2\sum_{\mu_n>0}\mu_n\psi_{n,1/2}w_n - B_{1/2}\phi_{1/2}\,, \tag{28}
$$

where

$$
B_{1/2} = \frac{\sum_{n=1}^{N}|\mu_n|\psi_{n,1/2}w_n}{\sum_{n=1}^{N}\psi_{n,1/2}w_n} \tag{29}
$$

is the boundary Eddington factor [9]. The equation for $\phi_{I+1/2}$ is

$$
J_{I,R} = J_{I+1/2}\,. \tag{30}
$$

where $J_{I,R}$ is defined in Eq. 23b, and $J_{I+1/2}$ is the right boundary current. For a reflective condition,

$$
J_{I+1/2} = 0\,. \tag{31}
$$

For a source condition,

$$J_{I+1/2} = B_{I+1/2}\phi_{I+1/2} - 2\sum_{\mu_n<0} |\mu_n|\psi_{n,I+1/2}w_n\,, \tag{32}$$

where

$$B_{I+1/2} = \frac{\sum_{n=1}^{N} |\mu_n|\psi_{n,I+1/2}w_n}{\sum_{n=1}^{N} \psi_{n,I+1/2}w_n}\,. \tag{33}$$

These transport-consistent, Marshak-like source boundary conditions are derived starting with the identity

$$J_{1/2} = j^+ - j^-\,, \tag{34}$$

where $j^\pm$ denotes the positive half-range currents associated with $\mu > 0$ and $\mu < 0$, respectively. For the left boundary condition, we simply perform the following algebraic manipulations:

$$J_{1/2} = j^+ - j^- = 2j^+ - (j^+ + j^-) = 2j^+ - \frac{j^+ + j^-}{\phi}\phi = 2j^+ - B_{1/2}\phi\,. \tag{35}$$

For the right boundary condition, we similarly obtain

$$J_{I+1/2} = j^+ - j^- = (j^+ + j^-) - 2j^- = \frac{j^+ + j^-}{\phi}\phi - 2j^- = B_{I+1/2}\phi - 2j^-\,. \tag{36}$$

Note that these source boundary conditions become equivalent to the standard Marshak boundary conditions if the S_N angular flux is isotropic. The resulting system of $2I + 1$ equations for the cell-center and cell-edge fluxes can be assembled into a matrix of both cell-center and cell-edge scalar fluxes and solved with a banded matrix solver of bandwidth five. The resulting drift-diffusion scalar flux can either be used as the final solution if the solution has converged or as an update to the LLDG S_N scattering term.

2.4 Increased Consistency Between LLDG and MFEM

The MFEM representation for the scalar flux is constant within a cell, but the LLDG representation for the scalar flux is linear. This suggests that improved accuracy of the S_N solution could be achieved by somehow constructing a linear scalar flux dependence from the MFEM solution. One simple method for doing this is to use the MFEM cell-edge scalar fluxes to compute a slope. This works quite well, for neutronics. However, it will be inadequate in a radiative transfer calculation because slopes must also be generated for the material temperatures, and an MFEM approximation for the temperatures will not include edge temperatures. We have chosen to use a more generally applicable approach based upon standard data reconstruction techniques that require only cell-centered values to compute slopes [10]. We also limit such slopes to avoid non-physical scalar fluxes. For example, the reconstructed left and right scalar fluxes in cell i are given by

$$\phi_{i,L/R} = \phi_i \mp \frac{1}{4}\xi_i \left(\Delta\phi_{i+1/2} + \Delta\phi_{i-1/2}\right) , \tag{37}$$

where ξ is a van Leer-type slope limiter [10]:

$$\xi_i = \begin{cases} 0, & r_i \leq 0 \, , \\ \min\left\{ \frac{2r_i}{1+r_i}, \frac{2}{1+r_i} \right\} , & r_i > 0 \end{cases} , \tag{38a}$$

$$r_i = \frac{\Delta\phi_{i-1/2}}{\Delta\phi_{i+1/2}} \, , \tag{38b}$$

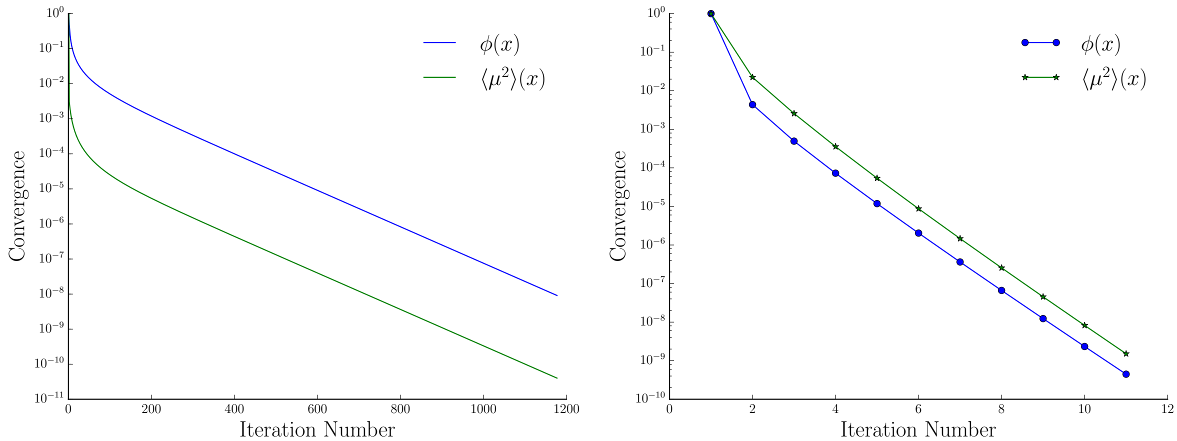

(a) (b)

Figure 3: The convergence rate for $\phi(x)$ and $\langle \mu^2 \rangle(x)$ for (a) unaccelerated and (b) VEF accelerated SI.

and

$$\Delta\phi_{i+1/2} = \phi_{i+1} - \phi_i \,, \tag{39a}$$

$$\Delta\phi_{i-1/2} = \phi_i - \phi_{i-1} \,. \tag{39b}$$

On the boundaries, we use

$$\phi_{1,L/R} = \phi_1 \mp \frac{1}{2}\Delta\phi_{3/2} \,, \tag{40a}$$

$$\phi_{I,L/R} = \phi_I \mp \frac{1}{2}\Delta\phi_{I-1/2} \,. \tag{40b}$$

We also set any negative left or right flux values in the boundary cells to zero by appropriately rotating the slopes.

3 Computational Results

To show the properties of the VEF method, a homogeneous test problem with a reflecting left boundary, vacuum right boundary, and a total thickness of 10 cm was used. This system was discretized into 50 spatial cells. The total and scattering macroscopic cross sections were set to $1\,\mathrm{cm}^{-1}$ and $0.99\,\mathrm{cm}^{-1}$ leading to a scattering ratio of $c = \sigma_s/\sigma_t = 0.99$. With 50 spatial cells the optical thickness per cell was 0.2 mfp and the domain thickness was 10 mfp. The fixed source was set to $1\,\frac{\text{particles}}{\text{s}-\text{steradian}}$. All calculations in this section were S_8 calculations and the scalar flux was point-wise converged for both the left and right discontinuous fluxes according to:

$$\frac{1}{1-\rho}\max\left[\phi_{i,L/R}^{\ell+1} - \phi_{i,L/R}^{\ell}\right] < 10^{-6}\,, \tag{41}$$

where

$$\rho = \frac{\|\phi^{\ell+1} - \phi^{\ell}\|_2}{\|\phi^{\ell} - \phi^{\ell-1}\|_2} \tag{42}$$

is an estimate for the spectral radius.

Figure 3a shows the iterative change defined as:

$$\frac{\|f^{\ell+1} - f^{\ell}\|_2}{\|f^{\ell+1}\|_2}\,, \tag{43}$$

as a function of unaccelerated iteration number for $f = \phi(x)$ and $f = \langle\mu^2\rangle(x)$. The Eddington factor's large drop in relative norm between the first and second iterations supports the claim that the angular shape of the angular flux, and thus the Eddington factor, converges rapidly. When compared to Fig. 3b, a plot of the iterative change for the VEF method, it is clear that the VEF method transfers the fast rate of convergence of the Eddington factor to the scalar flux.

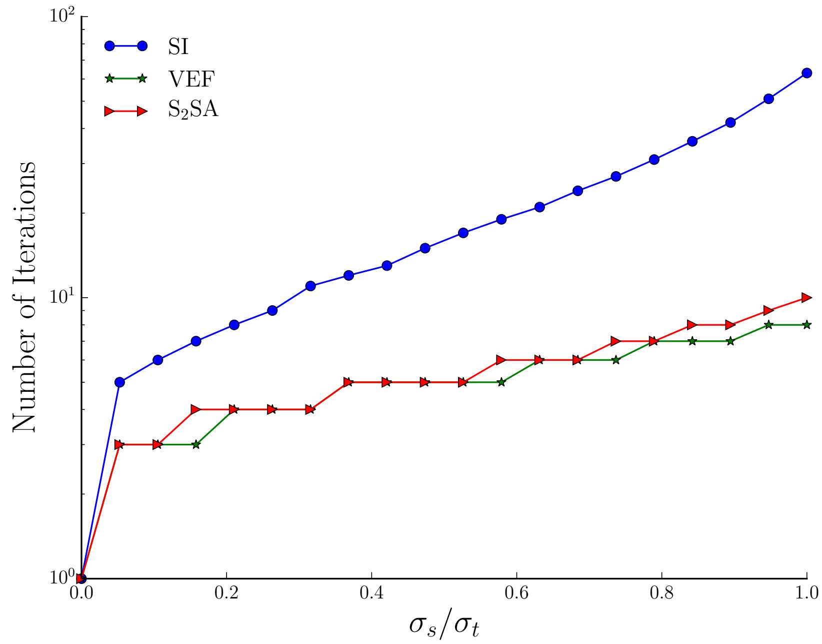

Figure 4: A comparison of the number of iterations required for Source Iteration, VEF acceleration, and S_2SA to converge for varying ratios of σ_s to σ_t.

Figure 4 shows the number of iterations required for convergence for unaccelerated SI, the VEF method, and consistently differenced S_2SA over a range of scattering ratios. The same homogeneous test problem was used. The ratio of unaccelerated to VEF accelerated iterations ranged from 1.6 to 8. This suggests that acceleration is occurring and that the VEF method is not just doing twice the amount of work per iteration. In addition, the VEF method performed similarly to S_2SA.

The Method of Manufactured Solutions (MMS) was used to compare the accuracy of the VEF method as the cell width was decreased. A solution to Eq. 2 was manufactured by using

$$\psi_{n,\mathrm{MMS}}(x) = \sin\left(\frac{\pi x}{x_b}\right) , \tag{44a}$$

$$\phi_{\text{MMS}}(x) = \sum_{n=1}^{N} \psi_{n,\text{MMS}}(x) w_n = 2\sin\left(\frac{\pi x}{x_b}\right) , \tag{44b}$$

in Eq. 2 and solving for $Q_n(x)$. This yields:

$$Q_{n,\text{MMS}}(x) = \mu_n \frac{\pi}{x_b} \cos\left(\frac{\pi x}{x_b}\right) + [\sigma_t(x) - \sigma_s(x)] \sin\left(\frac{\pi x}{x_b}\right) . \tag{45}$$

Using Eq. 45 as the fixed source in a numerical simulation forces the angular and scalar fluxes to the MMS solutions set in Eq. 44. The difference between the numerical and MMS solutions is then the spatial truncation error introduced by discretizing in space. To determine the order of accuracy of the VEF method, the L2 norm of the difference between the numerical and known MMS solutions were compared at five logarithmically spaced cell widths between 0.5 mm and 0.01 mm. A line of best fit of the form

$$E = Ch^n \tag{46}$$

was used to find the order of accuracy, n, and the constant of proportionality, C, of the numerical error, E. These values are provided in Table 1 for the VEF method with the flat and van Leer slope reconstruction scattering term update methods. The flat method is:

$$\phi_{i,L/R} = \phi_i , \tag{47}$$

where the left side is the scalar flux used to update the LLDG scattering term and the right side the cell-centered MFEM drift-diffusion scalar flux. The lower C value for VEF with van Leer reconstructed slopes suggests that constructing a linear scalar flux dependence from the MFEM drift-diffusion flux increases numerical accuracy. Both methods show second-order

Update Method	Order	C	R^2
Flat	1.997	1.12	9.9986×10^{-1}
van Leer	1.995	0.696	9.9933×10^{-1}

Table 1: The order of accuracy, error, and R^2 values for the permutations of the two Eddington representation methods and two slope reconstruction methods.

	Region 1	Region 2	Region 3	Region 4	Region 5
Q	10	0	0	0	1
σ_t	10	0.001	1	5	1
σ_a	10	0	0.1	0	0.1
Domain	$0 \leq x < 2$	$2 \leq x < 4$	$4 \leq x < 6$	$6 \leq x < 7$	$7 \leq x \leq 8$

Table 2: The cross sections and source used for Reed's problem.

accuracy as expected from the orders of accuracy of LLDG and constant-linear MFEM in isolation. This suggests that while slope reconstruction affects numerical accuracy it does not affect the order of accuracy of the method.

The difference between the S_N solution and the VEF method's drift-diffusion solution was compared as a function of cell width for the same homogeneous slab and for Reed's problem. S_2SA was used to generate the S_N solution that the VEF method was compared to. In both cases, the left boundary was reflecting and the right boundary was vacuum. The homogeneous slab had a scattering ratio of 0.99. The cross sections and source for Reed's problem are provided in Table 2. The L2 norm of the difference between the SI solution and VEF solution is plotted for the VEF method with flat and van Leer limited, cell-centered slope reconstruction scattering term update methods in Figs. 5a and 5b for the homogeneous slab problem and Reed's problem.

In the homogeneous problem, VEF with van Leer limited slope reconstruction was three times closer to the S_N solution than VEF without reconstruction. However, in Reed's problem, reconstruction did not affect the convergence of drift-diffusion to S_N. This could be

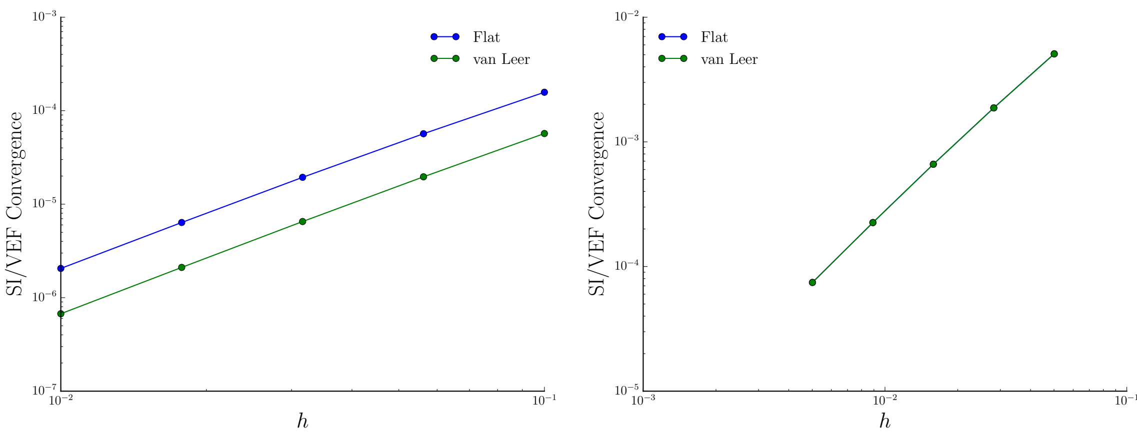

(a) (b)

Figure 5: The L2 norm of the difference between SI and the four permutations of the VEF method as the cell spacing is decreased for (a) the homogeneous slab problem and (b) Reed's problem.

from the cell-centered slope reconstruction method reaching across material discontinuities.

Lastly, the VEF method was tested in the diffusion limit. The cross sections and source were scaled as follows [11]:

$$\sigma_t(x) \to \sigma_t(x)/\epsilon\,, \tag{48a}$$

$$\sigma_s(x) \to \epsilon\sigma_s(x)\,, \tag{48b}$$

$$Q(x) \to \epsilon Q(x)\,. \tag{48c}$$

As $\epsilon \to 0$, the system becomes diffusive. The number of iterations for convergence as $\epsilon \to 0$ is plotted in Fig. 6. The error between the VEF solution and the exact diffusion solution is provided in Fig. 7. This supports the claim that the VEF method is robust as both scattering update methods properly preserved the thick diffusion limit.

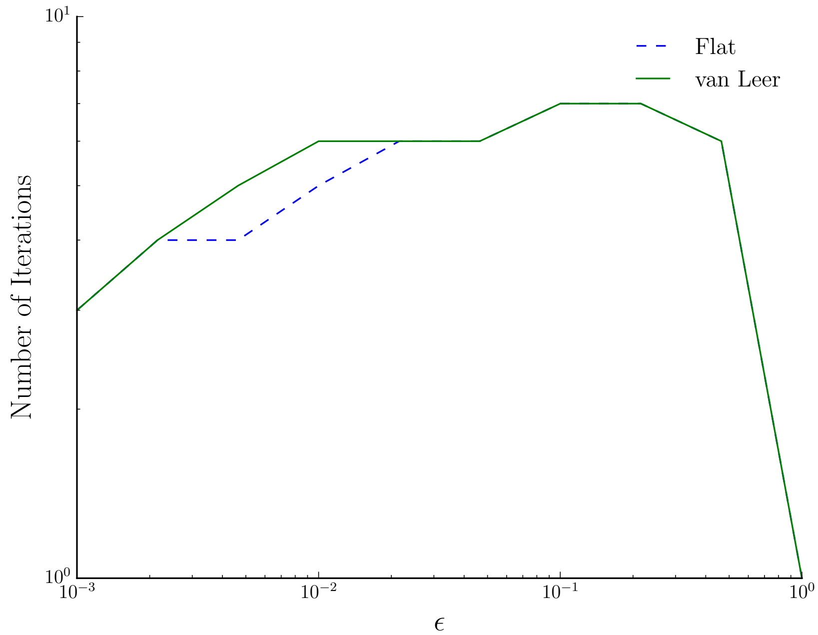

Figure 6: The number of iterations required for convergence for the permutations of slope reconstruction and angular flux representation in the diffusion limit.

4 Conclusions and Future Work

We have presented the VEF method for one-group neutron transport in slab geometry and the pairing of Lumped Linear Discontinuous Galerkin for the S_N transport step and the constant-linear Mixed Finite-Element Method for the drift diffusion acceleration step. We have numerically demonstrated that the LLDG/MFEM VEF method accelerates Source Iteration by transferring the rapid convergence of the angular shape of the angular flux to the scalar flux. In addition, the VEF method performed similarly to consistently differenced S_2SA.

Methods for increased consistency between LLDG and MFEM were also presented. This included a cell-centered slope reconstruction for constructing a linear scalar flux dependence

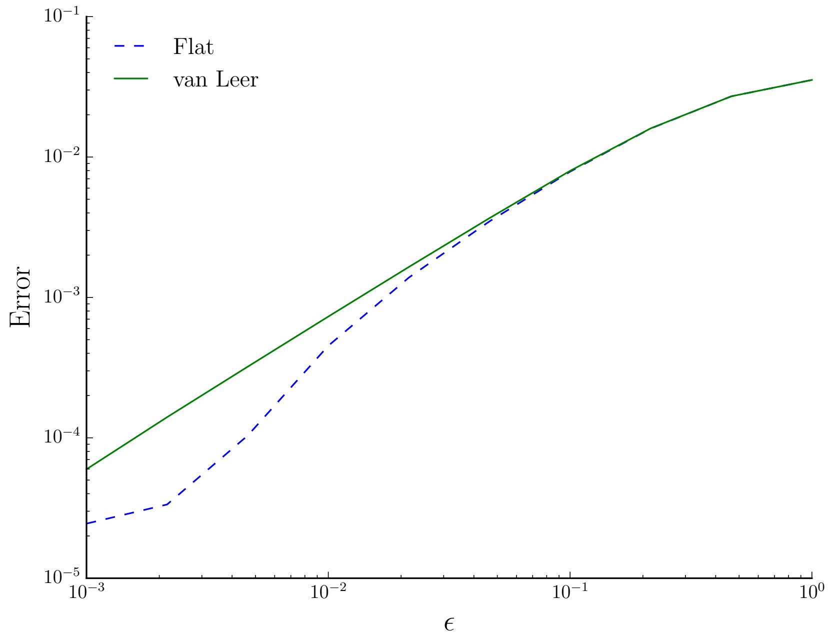

Figure 7: The error between the VEF methods and the exact diffusion solution as $\epsilon \to 0$.

from the drift-diffusion solution. It was shown that both the VEF methods with and without added consistency measures were second-order accurate as expected from the orders of accuracy of LLDG and MFEM in isolation and that all of the VEF methods were robust in the diffusion limit. In addition, while this nonlinear scheme produces two solutions, the S_N and drift-diffusion solutions were shown to converge as the mesh was refined for both homogeneous and inhomogeneous systems. Furthermore, the drift-diffusion solutions for the scalar flux and current are conservative and much less expensive and thus are the preferred solutions to compute quantities of interest. In addition, the S_N and VEF drift-diffusion equations can be discretized with arbitrarily different methods allowing the drift-diffusion discretization to match that of the other multiphysics components without degraded source iteration acceleration.

Future work includes extending the VEF method presented in this paper to the radiative transfer equations, verifying the VEF method in higher dimensions, and generalizing the method to higher order finite-elements.

References

[1] M.L. Adams and E.W. Larsen. Fast iterative methods for discrete-ordinates particle transport calculations. *Progress in Nuclear Energy*, 40(1):3–159, 2002.

[2] R.E. Alcouffe. Diffusion synthetic acceleration methods for the diamond-differenced discrete-ordinates equations. *Nuclear Science and Engineering*, 64:344–355, 1977.

[3] J.S. Warsa, T.A. Wareing, and J.E. Morel. Fully-consistent diffusion-synthetic acceleration of linear discontinuous s_n transport discretizations on unstructured tetrahedral meshes. *Nuclear Science and Engineering*, 141:235–251, 2002.

[4] J.E. Morel and E.W. Larsen. A multiple balance approach for differencing the s_n equations. *Nuclear Science and Engineering*, 105:1–15, 1990.

[5] Marvin L. Adams and William R. Martin. Diffusion synthetic acceleration of discontinuous finite element transport iterations. *Nuclear Science and Engineering*, 111:145–167, 1992.

[6] Yaqi Wang and Jean C. Ragusa. Diffusion synthetic acceleration for high-order discontinuous finite element s_n transport schemes and application to locally refined unstructured meshes. *Nuclear Science and Engineering*, 166(2):145–166, 2010.

[7] Edward W. Larsen, J.E. Morel, and Warren F. Miller, Jr. Asymptotic solutions of numerical transport problems in optically thick, diffusive regimes. *Journal of Computational Physics*, 69:283–324, 1987.

[8] V. Dobrev, Tz. Kolev, and R. Rieben. High-order curvilinear finite element methods for lagrangian hydrodynamics. *SIAM Journal on Scientific Computing*, 34:B606–B641, 2012.

[9] M.M. Miften and E.W. Larsen. The quasi-diffusion method for solving transport problems in planar and spherical geometries. *Journal of Transport Theory and Statistical Physics*, 22(2-3):165–186, 1992.

[10] B. van Leer. Towards the ultimate conservative difference scheme I: The quest for monotonicity. *Lecture Notes in Physics*, 18:163–168, 1973.

[11] Edward W. Larsen, J.E. Morel, and Jr. Warren F. Miller. Asymptotic solutions of numerical transport problems in optically thick, diffusive regimes. *Journal of Computational Physics*, 69:283–324, 1987.